TU Delft

Delft University of Technology

Document Version
Final published version

Licence
CC BY

Citation (APA)
Natu, A., & HosseinNia, H. (2027). Narrow-band active damping using higher-order band-pass control: A loop-shaping perspective. *Control Engineering Practice*, *178*, Article 107318. https://doi.org/10.1016/j.conengprac.2026.107318

Important note
To cite this publication, please use the final published version (if applicable).
Please check the document version above.

Copyright
In case the licence states “Dutch Copyright Act (Article 25fa)”, this publication was made available Green Open Access via the TU Delft Institutional Repository pursuant to Dutch Copyright Act (Article 25fa, the Taverne amendment). This provision does not affect copyright ownership.
Unless copyright is transferred by contract or statute, it remains with the copyright holder.

Sharing and reuse
Other than for strictly personal use, it is not permitted to download, forward or distribute the text or part of it, without the consent of the author(s) and/or copyright holder(s), unless the work is under an open content license such as Creative Commons.

Takedown policy
Please contact us and provide details if you believe this document breaches copyrights.
We will remove access to the work immediately and investigate your claim.

This work is downloaded from Delft University of Technology.

Control Engineering Practice 178 (2027) 107318

Contents lists available at ScienceDirect

Control Engineering Practice

journal homepage: www.elsevier.com/locate/conengprac

Narrow-band active damping using higher-order band-pass control: A loop-shaping perspective

Aditya Natu *, Hassan HosseinNia

Department of Precision and Microsystems Engineering, Faculty of Mechanical Engineering, Delft University of Technology, Mekelweg 2, Delft, 2628 CD, the Netherlands

ARTICLE INFO

Keywords:
Active damping control
Band-pass controller
Loop-shaping design
Resonance suppression
Noise attenuation
Spillover reduction
Modal selectivity
Flexible structures
Nanopositioning

ABSTRACT

Lightly damped structural resonances limit the performance of high-precision mechatronic systems and flexible structures. Conventional active damping schemes, such as positive and negative position feedback, provide moderate damping at the targeted mode but often suffer from spillover at low and high frequencies, especially in systems with closely spaced modes or high noise sensitivity. This paper presents a generalized higher-order band-pass active damping framework that enhances modal selectivity and stability for narrow-band damping. Analytical formulations establish relationships between controller order, band-pass slope characteristics, and stability margins, enabling systematic design with high phase robustness. A non-minimum-phase filter is incorporated to compensate for delay-induced phase degradation, while a tunable damping coefficient increases design flexibility. The framework is evaluated experimentally on a collocated nanopositioning system, through closed-loop simulations using an experimentally identified non-collocated beam response, and through a numerical study of closely spaced resonances. The results demonstrate that the proposed controller achieves sharp resonance suppression, improved noise attenuation, reduced spillover compared to conventional active damping schemes and modal selectivity distinguishing preservation of untargeted resonance peaks from aggregate vibration reduction.

1. Introduction

Active damping control is widely used to suppress structural resonances and enhance dynamic performance in mechanical and mechatronic systems. Unlike passive damping, which relies on material properties or added components, active damping employs feedback to introduce effective damping in lightly damped modes, reducing vibration and improving transient response without hardware modifications (Balas, 1978; Preumont, 2002). This capability is crucial in high-precision systems such as wafer scanners, atomic force microscopes, and piezo-actuated stages, where structural resonances limit bandwidth and positioning accuracy (Fleming, 2009; Heertjes et al., 2020; Oomen, 2018). Similar benefits extend to large-scale flexible structures, including aerospace vehicles, bridges, and robotic manipulators, where active damping enhances stability and vibration suppression (Fanson & Caughey, 1990; Housner et al., 1997).

Active damping is a low-authority control (LAC) strategy based on low-order, fixed-structure controllers that require only approximate knowledge of dominant natural frequencies. Their simplicity enables robust, practical implementation in lightly damped systems (Chen et al., 2021). Within this framework, several position- or derivative-based feedback controllers have been developed. Basic schemes, such as lead compensators or direct velocity feedback, provide phase lead near resonance but often require high gain, amplifying undesired high-frequency dynamics. To mitigate this, Negative Position Feedback (NPF) introduces a second-order high-pass filter that concentrates gain around the targeted mode while attenuating higher frequencies (Cazzulani et al., 2012). However, its high-pass nature can degrade performance in noise-sensitive or multi-mode systems. Conversely, Positive Position Feedback (PPF) employs a second-order low-pass filter that increases damping at the resonance without exciting higher modes (Fanson & Caughey, 1990). Yet, its low-frequency compliance limits disturbance rejection. Various extensions, such as PVPF, PAVPF, and resonant controllers, improve tuning flexibility but remain constrained by their inherent frequency-domain selectivity (Bhikkaji et al., 2007; Li et al., 2017; Ling et al., 2019).

To mitigate low- and high-frequency spillover and improve modal selectivity, band-pass filters have been proposed as natural extensions of conventional active damping controllers. To the best of the author's knowledge, classical designs typically exhibit magnitude slopes of about ±20 dB/decade in the low- and high-frequency regions, concentrating control effort around the targeted resonance while maintaining low

* Corresponding author.
E-mail address: A.M.Natu@tudelft.nl (A. Natu).

https://doi.org/10.1016/j.conengprac.2026.107318
Received 24 July 2026; Received in revised form 19 October 2026; Accepted 21 October 2026
Available online 28 October 2026
0967-0661/© 2026 The Author(s). Published by Elsevier Ltd. This is an open access article under the CC BY license (http://creativecommons.org/licenses/by/4.0/).

gain elsewhere. Such band-pass controllers have been successfully applied for damping resonance modes in flexible structures (Hyodo & Yabuno, 2023; Wu et al., 2018), high-speed drive systems (Pawlenka et al., 2019; Song et al., 2016), and piezo-actuated nanopositioners (Zhu et al., 2016). More recently, negative derivative feedback controllers with second-order band-pass characteristics have been optimized using maximum-damping, $\mathcal{H}_2$, and $\mathcal{H}_\infty$ criteria (Jamshidi & Collette, 2022a,b), as well as selective feedback using collaborative smart dampers (Debattisti et al., 2023).

However, in systems with closely spaced modes, these moderate slopes often fail to fully isolate the targeted resonance, leading to residual spillover and degraded performance. Furthermore, when strong noise attenuation through the feedback loop is required, conventional designs offer limited effectiveness. Modal selectivity is particularly relevant when an untargeted mode serves an operational or sensing function, as in resonant piezoelectric ultrasonic motors and bimodal atomic force microscopy, where selected vibration modes are deliberately excited (Ebeling & Solares, 2013; Liu et al., 2016). In such applications, unintended attenuation, as well as amplification, can modify a response intended to be preserved. Preserving untargeted resonances, therefore, constitutes a distinct objective from reducing the overall vibration response. These limitations motivate the present work, which develops higher-order narrow-band-pass (NBP) controllers with sharper slopes to achieve stronger modal selectivity, improved disturbance rejection, and enhanced noise attenuation.

This paper introduces a general higher-order narrow-band-pass active damping framework with the following key contributions:

1. Formulation of a generalized band-pass controller of arbitrary order, consistent with loop-shaping principles, enabling narrow-band damping of targeted resonances.
2. Analytical formulations quantifying the effect of slope order on stability margins and damping performance, with design modifications ensuring stability and high phase margins.
3. Extension of controller design incorporating non-minimum-phase (NMP) filter-based delay compensation and a tunable damping coefficient for increased flexibility.
4. Experimental evaluation on a collocated nanopositioning system, closed-loop simulations using an experimentally identified non-collocated beam response, and a numerical study of closely spaced resonances, to assess damping, noise attenuation, spillover, and modal selectivity.

The present work builds on two earlier developments by the authors. Natu and Hosseinnia (2026a) introduced a non-minimum-phase resonant controller tailored to piezoelectric nanopositioning dynamics, primarily to damp the dominant resonance and enable higher bandwidths with conventional motion controllers. Natu and HosseinNia (2026b) introduced NMP-filter-based delay compensation for existing linear damping controllers and a parallel control structure for multimode damping. The contribution here is a generalized, tunable higher-order band-pass damping controller, with an analysis of the trade-off between frequency selectivity and phase margins, to reduce noise transmission and spillover while maintaining targeted resonance suppression.

Throughout this paper, collocation refers to an actuator–sensor configuration in which actuation and sensing share the same generalized mechanical coordinate, whereas non-collocation refers to a configuration in which these coordinates are distinct.

The remainder of the paper is organized as follows. Section 2 presents the loop-shaping methodology and analytical formulations for stability, damping performance, and parameter tuning. Section 3 demonstrates case studies for collocated and non-collocated systems, and Section 4 concludes the paper.

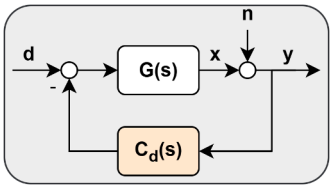


Fig. 1. Closed-loop control architecture for active damping control.

2. Band-pass control design methodology

This section presents the design methodology for developing band-pass active damping controllers. The discussion begins with an overview of loop-shaping principles applied to active damping control, followed by an extension to a generalized band-pass control structure of arbitrary slope order.

The closed-loop control configuration employed in this study is illustrated in Fig. 1, where the active damping controller $C_d(s)$ is implemented within a negative feedback loop. In this framework, d denotes the exogenous input disturbance, n represents the exogenous output disturbance, including noise, y corresponds to the measured output, and x denotes the performance output.

Without loss of generality, the subsequent theoretical developments are based on a standard second-order system model $G(s)$ defined as

$$G(s) = \frac{\omega_n^2}{s^2 + 2\zeta_n\omega_n s + \omega_n^2}, \tag{1}$$

where ω_n denotes the resonance frequency of the system, and ζ_n represents the corresponding damping ratio.

2.1. Loop shaping for active damping

This subsection outlines the loop-shaping methodology for active damping control, wherein the open-loop response is strategically shaped to achieve the desired closed-loop performance. The formulation presented herein is adapted from the author's prior work (Natu & HosseinNia, 2026b), and is concisely summarized to ensure the paper remains self-contained and complete.

In Fig. 1, the open-loop transfer function $\mathcal{L}(s)$ is defined as

$$\mathcal{L}(s) = G(s)C_d(s). \tag{2}$$

The closed-loop transfer function $S_{yn}(s)$, mapped from output disturbance n to the measured output y, is expressed as:

$$S_{yn}(s) = \frac{1}{1 + G(s)C_d(s)} = \frac{1}{1 + \mathcal{L}(s)}. \tag{3}$$

The closed-loop transfer function $S_{xn}(s)$, which maps the output disturbance n to the performance output x, is expressed as

$$S_{xn}(s) = \frac{-G(s)C_d(s)}{1 + G(s)C_d(s)} = S_{yn}(s) - 1. \tag{4}$$

Similarly, the closed-loop transfer function $\mathcal{PS}_{xd}(s)$, which maps the input disturbance d to the performance output x, is given by

$$\mathcal{PS}_{xd}(s) = \frac{G(s)}{1 + G(s)C_d(s)} = G(s)S_{yn}(s). \tag{5}$$

The principal objective of the control scheme is to attenuate the resonance peak at the system's natural frequency ω_n, while ensuring minimal influence on the remaining system dynamics and effectively suppressing the propagation of noise to the performance output. To achieve the desired closed-loop characteristics of $\mathcal{PS}_{xd}(s)$ and $S_{xn}(s)$, the open-loop transfer function $\mathcal{L}(s)$ must satisfy the following gain conditions:

$$\begin{aligned} &|\mathcal{L}(s)| \gg 1 \quad \big| \quad |\mathcal{PS}_{xd}(s)| \ll |G(s)| \qquad \text{at } \omega \approx \omega_n, \\ &|\mathcal{L}(s)| \ll 1 \quad \big| \quad |S_{xn}(s)| \approx 0 \qquad\qquad \forall\ \omega \neq \omega_n. \end{aligned} \tag{6}$$

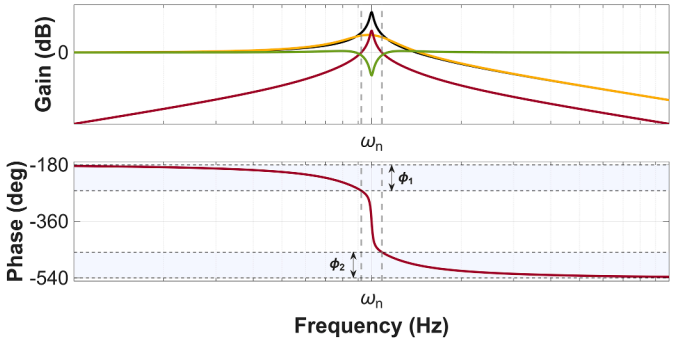


Fig. 2. Schematic illustration of loop shaping methodology for active damping control, presenting frequency response plots of system $G(s)$ (—), open-loop function $\mathcal{L}(s)$ (—), and closed-loop functions $S_{yn}(s)$ (—) and $\mathcal{PS}_{xd}(s)$ (—).

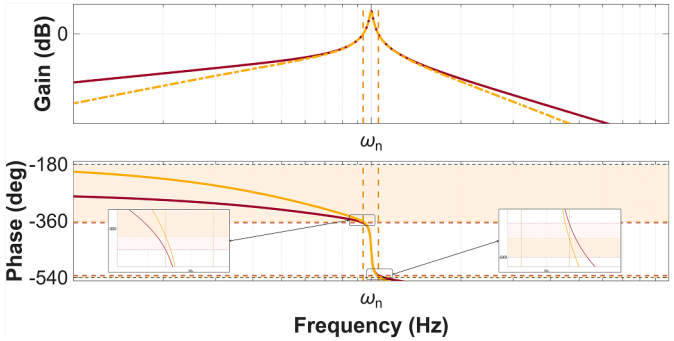


Fig. 3. Loop shaping with band-pass damping control, presenting frequency response plots of open-loop function $\mathcal{L}(s)$ with controller slope order $n = 1$ (—) and $n = 2$ (—).

These conditions correspond to an idealized triangular loop-gain profile, where the gain exceeds unity within a finite frequency band, giving rise to two crossover frequencies defined as

$$\omega_{c_i} := \{\omega \mid \omega \in \mathbb{R} \text{ and } |G(j\omega_{c_i})C_d(j\omega_{c_i})| = 1\}, i = 1, 2. \tag{7}$$

For closed-loop stability, the open-loop system must satisfy the following phase conditions, where $k \in \mathbb{Z}$ and $\omega_{c_1} < \omega_{c_2}$:

$$\begin{aligned} &\angle G(j\omega_{c_1})C_d(j\omega_{c_1}) + (2k+1)\pi \le 0, \\ &\angle G(j\omega_{c_2})C_d(j\omega_{c_2}) + (2k+3)\pi \ge 0. \end{aligned} \tag{8}$$

Fig. 2 schematically illustrates the loop-shaping methodology described above. In practice, to ensure a well-damped response around ω_n and a smooth transition across the crossover frequencies ω_{c_i} in $\mathcal{PS}_{xd}(s)$, it is desirable for the phase margins ϕ_i at ω_{c_i} to exceed 60°, which prevents amplification relative to the plant at the unity-gain crossover frequencies and helps limit nearby closed-loop peaking.

Remark 1. The second-order model illustrates the loop-shaping principle and provides a basis for the subsequent analytical results. For higher-order plants, the same objective of locally increasing the open-loop gain around the targeted resonance is pursued using the complete plant frequency response. Additional dynamics may introduce multiple unity-gain crossovers, all of which must be assessed. At each crossover, the unwrapped phase of $\mathcal{L}(s)$ must lie within the appropriate phase band, with the phase margin evaluated relative to the corresponding critical phase boundary. A minimum phase margin of 60° is adopted as a design requirement to ensure robustness.

Remark 2. When multiple resonances require damping, the proposed approach can be applied sequentially using parallel damping controllers, each targeting one mode. Let $\mathcal{PS}_{xd,0}(s) = G(s)$. At iteration i, the controller $C_{d,i}(s)$ is designed using $\mathcal{PS}_{xd,i-1}(s)$ as the effective plant, yielding

$$\mathcal{PS}_{xd,i}(s) = \frac{\mathcal{PS}_{xd,i-1}(s)}{1 + C_{d,i}(s)\mathcal{PS}_{xd,i-1}(s)} = \frac{G(s)}{1 + G(s)\sum_{k=1}^{i} C_{d,k}(s)}. \tag{9}$$

Thus, each design accounts for the dynamics modified by the previously introduced controllers. After targeting N modes, the implemented damping controller is $C_d(s) = \sum_{i=1}^{N} C_{d,i}(s)$. Since the controller responses may overlap, particularly for closely spaced modes, previously achieved damping and robustness must be reassessed after each addition, with joint retuning where necessary. Stability must be verified for the combined system, and the prescribed phase-margin requirements must be checked at all gain-crossover frequencies of the combined loop $\mathcal{L}(s) = G(s)C_d(s)$.

2.2. Loop shaping with band-pass controller

In this subsection, the previously illustrated loop-shaping methodology is extended to a generalized band-pass controller of arbitrary slope order n. For a fixed maximum gain $M > 0$, the controller of any slope order can be defined as

$$C_d(s) = g(n)\left(\frac{s}{(s+\omega_c)^2}\right)^n, \tag{10}$$

where $g(n) = M(2\omega_c)^n$, and the band-pass corner frequency ω_c is typically tuned to coincide with the system's resonance frequency, i.e., $\omega_c = \omega_n$. The resulting band-pass controller, as defined in Eq. (10), is designed to exhibit a magnitude slope expressed as:

$$\begin{aligned} \frac{d(20\log_{10}|C_d(j\omega)|)}{d(\log_{10}\omega)} &= +20n \text{ dB/dec} \quad \forall\ \omega \ll \omega_c, \\ \frac{d(20\log_{10}|C_d(j\omega)|)}{d(\log_{10}\omega)} &= -20n \text{ dB/dec} \quad \forall\ \omega \gg \omega_c, \end{aligned} \tag{11}$$

As discussed in Section 1, the controller slope order n is increased to achieve steeper magnitude slopes when a narrower band-pass control action is desired. This is particularly advantageous when addressing systems with closely spaced resonance modes or when strong attenuation of noise transmission through the feedback loop is required.

For the second-order system $G(s)$ (Eq. (1)) combined with the proposed band-pass damping controller $C_d(s)$ (Eq. (10)), the resulting open-loop shaping is illustrated in Fig. 3, for two representative controller slope orders, $n = 1$ and $n = 2$. It can be observed that the proposed band-pass structure effectively conforms to the ideal triangular loop-gain profile, with stability margins evaluated at the two crossover frequencies $\omega_{c_{1,2}}$ of $\mathcal{L}(s)$.

Given that the magnitude slope of $C_d(s)$ is $\pm 20n$ dB/dec and that the plant exhibits a roll-off of −40 dB/dec beyond the resonance, a pronounced phase transition occurs around ω_n. Consequently, the phase margin ϕ_2 at the higher crossover frequency ω_{c_2} is significantly smaller than the phase margin ϕ_1 at ω_{c_1}. Although the open-loop stability conditions in Eq. (8) remain satisfied, the reduced ϕ_2 leads to a pronounced resonance peak in $\mathcal{PS}_{xd}(s)$ near ω_{c_2}. A strategy to mitigate this loss of phase margin will be introduced in Section 2.3.

2.3. Governing stability margins via open-loop slope order

As established in Section 2.2, for a band-pass controller $C_d(s)$ designed to exhibit equal magnitude slopes ($\left|\frac{d(20\log_{10}|C_d(j\omega)|)}{d(\log_{10}\omega)}\right| = 20n$ dB/dec $\forall\ \omega \ll \omega_c$ and $\omega \gg \omega_c$), the resulting open-loop system typically exhibits a small phase margin ϕ_2 at the higher crossover frequency ω_{c_2} (beyond ω_n). This occurs due to the sharp phase transition induced by the low damping ratio ζ_n and the second-order roll-off of the plant $G(s)$, which introduces a −40 dB/dec slope after ω_n. Consequently, the achievable controller order n is inherently limited by the stability conditions in Eq. (8), as increasing n further would compromise closed-loop stability. This will be discussed in Section 2.7

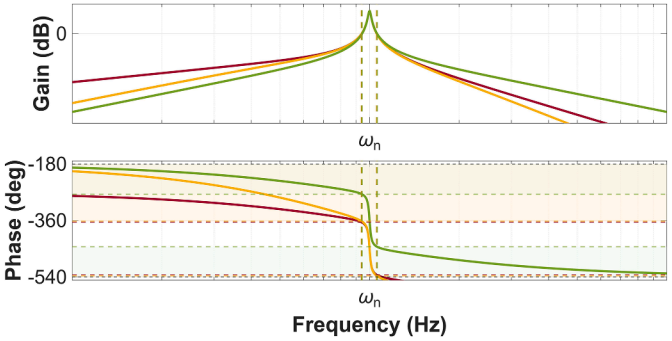


Fig. 4. Loop shaping with band-pass damping control designed to ensure equal open-loop slope order before and after targeted resonance frequency, presenting frequency response plots of open-loop function $\mathcal{L}(s)$ with controller slope order $n = 1, m = 0$ (—), $n = 2, m = 0$ (—), and $n = 2, m = 2$ (—).

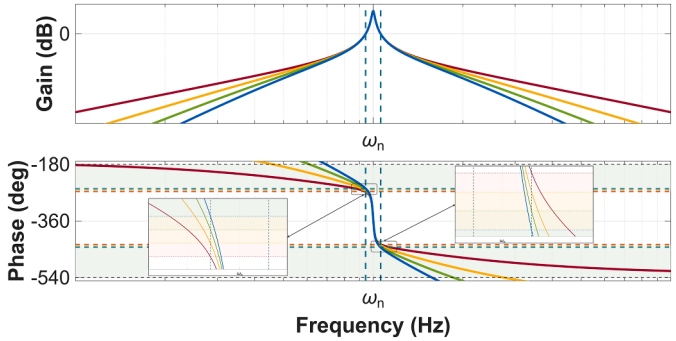


Fig. 5. Illustration of loop shaping with band-pass damping control designed to ensure equal open-loop slope order before and after targeted resonance frequency, presenting frequency response plots of open-loop function $\mathcal{L}(s)$ with increasing controller slope orders $n = 2, m = 2$ (—), $n = 3, m = 2$ (—), $n = 4, m = 2$ (—), and $n = 5, m = 2$ (—).

To mitigate this limitation in the loop-shaping process, it is advantageous to design the band-pass controller such that the open-loop function $\mathcal{L}(s)$ exhibits equal slope magnitudes on both sides of the targeted resonance frequency. For a system characterized by a high-frequency roll-off as defined in Eq. (1), this can be achieved by introducing a high-pass component with slope order m into the controller structure. Accordingly, the generalized form of the improved band-pass controller $C_d(s)$ is expressed as

$$C_d(s) = g(n)\left(\frac{s}{(s+\omega_c)^2}\right)^n \cdot h(m)\big(s+\omega_c\big)^m, \tag{12}$$

where $g(n) = M(2\omega_c)^n$ and $h(m) = 2^{-m/2}\omega_c^{-m}$ ensure a fixed maximum gain $M > 0$ for any combination of slope orders (n, m).

The slope order m is selected according to the slope characteristics of the plant $G(s)$ around the resonance frequency. For example, in the case of the second-order system $G(s)$ defined in Eq. (1), the plant exhibits a -40 dB/dec roll-off beyond ω_n. To achieve equal open-loop slope magnitudes on either side of the resonance, a slope order of $m = 2$ is therefore selected, providing an additional +40 dB/dec slope before resonance through the band-pass controller $C_d(s)$. In general, the slope order $m \in \mathbb{Z}$ is chosen such that:

$$\left|\frac{d(20\log_{10}|\mathcal{L}(j\omega)|)}{d(\log_{10}\omega)}\right|_{\omega\ll\omega_n} = \left|\frac{d(20\log_{10}|\mathcal{L}(j\omega)|)}{d(\log_{10}\omega)}\right|_{\omega\gg\omega_n}. \tag{13}$$

This behavior is illustrated in Fig. 4, where the cases shown in Fig. 3 are compared with the modified band-pass controller incorporating the additional high-pass element. It can be observed that this modification effectively restores the phase margins $\phi_{1,2}$, primarily due to the phase advancement introduced by the high-pass component in the controller. This phase shift allows the open-loop system to maintain higher stability margins while preserving the desired gain characteristics, a property that holds for any controller slope order n.

With the introduction of the modified band-pass controller, the design becomes significantly more effective in achieving high phase margins, thereby enhancing both stability and closed-loop performance. The additional phase shift introduced by the high-pass element provides increased flexibility to raise the controller slope order n without compromising stability. Fig. 5 illustrates this effect, demonstrating that higher slope orders can be attained while maintaining sufficiently large phase margins, even for steeper magnitude slopes of the controller. However, as established in Proposition 1, the controller order cannot be increased indefinitely; nevertheless, the modified structure offers substantially greater freedom before the desired stability margin of 60° is no longer satisfied.

2.4. Closed-loop damping performance

In the preceding sections, the design methodology for shaping the open-loop function $\mathcal{L}(s)$ has been developed and illustrated. In this subsection, the resulting closed-loop damping performance, as characterized by $\mathcal{PS}_{xd}(s)$, is analytically derived at the targeted resonance frequency ω_n for the controller structure presented in Eq. (12).

For the system $G(s)$ defined in Eq. (1) and the band-pass controller $C_d(s)$ in Eq. (12), tuned such that $\omega_c = \omega_n$, the magnitude and phase of each at ω_n are obtained as

$$\begin{aligned} |G(j\omega_n)| &= \frac{1}{2\zeta_n}, \qquad \arg G(j\omega_n) = -\frac{\pi}{2}, \\ |C_d(j\omega_n)| &= M, \qquad \arg C_d(j\omega_n) = \frac{m\pi}{4}. \end{aligned} \tag{14}$$

Accordingly, for the open-loop function $\mathcal{L}(s) = G(s)C_d(s)$, the magnitude and phase at ω_n are expressed as

$$|\mathcal{L}(j\omega_n)| = \frac{M}{2\zeta_n} =: \alpha, \ \arg\mathcal{L}(j\omega_n) = -\frac{\pi}{2} + \frac{m\pi}{4} =: \phi_{\mathcal{L}}. \tag{15}$$

The term $|1 + \mathcal{L}(s)|$ can then be evaluated as

$$|1+\mathcal{L}(j\omega_n)| = \sqrt{1+\alpha^2+2\alpha\cos\phi_{\mathcal{L}}} = \sqrt{1+\alpha^2+2\alpha\sin\left(\tfrac{m\pi}{4}\right)}. \tag{16}$$

Hence, the closed-loop magnitude of $\mathcal{PS}_{xd}(s) = \frac{G(s)}{1+\mathcal{L}(s)}$ at ω_n, representing the damping performance, is obtained as

$$\left|\mathcal{PS}_{xd}(j\omega_n)\right| = \frac{1}{2\zeta_n} \Big/ \sqrt{1+\left(\frac{M}{2\zeta_n}\right)^2 + 2\left(\frac{M}{2\zeta_n}\right)\sin\left(\tfrac{m\pi}{4}\right)}. \tag{17}$$

2.5. Band-pass damping control with delay compensation

Thus far, the analysis in the preceding sections has been carried out under the assumption of a delay-free system. However, in practical applications, this assumption rarely holds. In this subsection, a system incorporating a pure time delay is considered, represented as $G(s)e^{-\tau s}$, where τ denotes the time delay.

The presence of a time delay introduces an additional phase lag that increases monotonically with frequency. For the band-pass damping controller designed to maintain stable phase margins, such a delay can be detrimental, as it reduces the available phase margin, particularly at the higher crossover frequency, potentially leading to performance degradation or even closed-loop instability. To mitigate this effect and preserve adequate phase margins, a non-minimum-phase (NMP) filter is introduced in series with the damping controller $C_d(s)$. This general compensation approach is adapted from the author's previous work (Natu & HosseinNia, 2026b) and is here extended to the proposed band-pass damping framework.

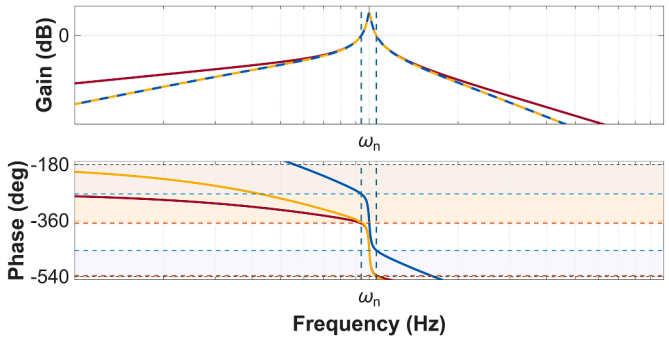


Fig. 6. Illustration of loop shaping with band-pass damping control in the presence of system delay $e^{-\tau s}$, presenting frequency response plots of open-loop function $\mathcal{L}(s)$ with controller slope orders $n = 1, m = 0$ (—), $n = 2, m = 0$ (—), and with delay compensated controller $n = 2, m = 0$ (—).

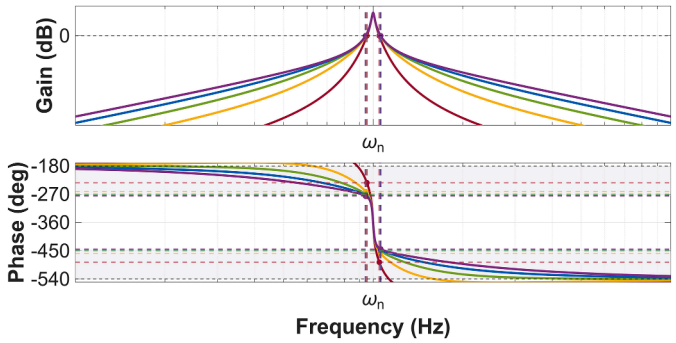


Fig. 7. Illustration of influence of ζ_c on the open-loop response $\mathcal{L}(s)$ and phase margins for $n = m = 2$: $\zeta_c = 0.1$ (—), 0.3 (—), 0.5 (—), 0.7 (—), and 0.9 (—).

Accordingly, the delay-compensated damping controller is expressed as

$$C_d(s) = \underbrace{g(n)\left(\frac{s}{(s+\omega_c)^2}\right)^n \cdot h(m)(s+\omega_c)^m}_{\text{Band-Pass Damping Controller}} \cdot \underbrace{\sigma\left(\frac{s-\omega_d}{s+\omega_d}\right)}_{\text{NMP Filter}}, \tag{18}$$

where ω_d denotes the corner frequency of the NMP filter, and the sign $\sigma \in \{+1, -1\}$ is selected to satisfy the phase condition in Eq. (8) around the targeted mode. This selection accounts for the local system dynamics, including the pole–zero interlacing associated with collocated or non-collocated system dynamics, the minimum- or non-minimum-phase behavior of the system, and the adopted closed-loop feedback configuration (negative or positive).

Fig. 6 illustrates the open-loop function with delay, $\mathcal{L}(s) = G(s)e^{-\tau s}C_d(s)$, where the results from Fig. 3 are compared with those obtained using the delay-compensated band-pass damping controller defined in Eq. (18). Owing to the fact that the NMP filter introduces a phase transition from 180° to 0° as the frequency varies from 0 to $2\omega_d$, it effectively advances the phase of the open-loop response $\mathcal{L}(s)$, thereby restoring the phase margins as illustrated. For a more detailed illustrative explanation of this method, readers are referred to the author's earlier work (Natu & HosseinNia, 2026b).

Remark 3. It should be noted that a similar phase-shifting effect was observed when employing the high-pass element in the modified band-pass damping controller presented in Eq. (12). Although introducing this element can achieve the desired phase margins, in the presence of a significant time delay, a higher slope order m is required to maintain stability. While this results in a favorable increase in the controller's magnitude slope, it also leads to a substantially higher overall controller order. Consequently, this may impose practical limitations for systems constrained by hardware or computational resources, rendering such designs infeasible beyond a certain point. In contrast, the NMP filter–based approach effectively restores comparable phase margins without altering the controller's gain characteristics across the frequency spectrum. Therefore, the selection between these two methods should be made based on the specific system characteristics, including the proximity of resonance modes and the magnitude of the inherent time delay.

2.6. Band-pass control with tunable damping coefficient

The band-pass damping controller formulations presented in Eqs. (10) and (12) are essentially designed assuming a damping coefficient ζ_c equal to unity. While these configurations provide steeper magnitude slopes outside the targeted frequency range, it may also be desirable to introduce additional flexibility in shaping the closed-loop damping behavior. Specifically, one may wish to achieve a sharper gain characteristic around ω_n without necessarily increasing the overall controller gain dictated by $g(n)$ and $h(m)$, which otherwise amplifies the response across the entire frequency spectrum.

To incorporate this additional design flexibility, the band-pass controller can be reformulated to include a tunable damping coefficient ζ_c, expressed as

$$C_d(s) = g(n)\left(\frac{s}{s^2 + 2\zeta_c\omega_c s + \omega_c^2}\right)^n \cdot h(m)\left(s+\omega_c\right)^m, \tag{19}$$

where $g(n) = M(2\zeta_c\omega_c)^n$ and $h(m) = 2^{-m/2}\omega_c^{-m}$ ensure a fixed maximum gain $M > 0$ for any combination of slope orders (n, m).

The closed-loop damping performance $\mathcal{PS}_{xd}(s)$ at the targeted resonance frequency ω_n can be derived in a manner analogous to the formulation presented in Section 2.4, and is expressed as:

$$\left|\mathcal{PS}_{xd}(j\omega_n)\right| = \frac{1}{2\zeta_n} \Bigg/ \sqrt{1 + \left(\frac{M}{2\zeta_n}\right)^2 + 2\left(\frac{M}{2\zeta_n}\right)\sin\left(\tfrac{m\pi}{4}\right)}. \tag{20}$$

It can be observed that, for the same fixed controller gain $M > 0$, the achievable damping performance at the resonance frequency ω_n remains unchanged. However, variations in the response are expected in the frequency range around the resonance, owing to the modified shape of the damping controller in this band. These variations arise from the additional design flexibility introduced by the tunable damping coefficient ζ_c.

Although ζ_c leaves the target frequency response unchanged for fixed M and $\omega_c = \omega_n$, it substantially modifies the shape of the surrounding and out-of-band loop. Fig. 7 illustrates this effect for $n = m = 2$ at a common open-loop peak gain. A reduction in ζ_c results in a narrower high-gain region and diminished out-of-band gain, while leaving the asymptotic slopes unchanged. This adjustment provides additional flexibility to mitigate spillover effects and limit noise transmission, particularly when implementation constraints restrict the achievable controller order. This selectivity comes at the expense of reduced phase margins. The illustrated dependence is nonlinear, with the margins becoming more sensitive to changes in ζ_c at lower values of ζ_c. Consequently, ζ_c and M should be selected jointly to improve frequency selectivity, subject to the prescribed phase-margin constraints.

Remark 4. In practical implementations, the controller parameters—namely the gain M and damping coefficient ζ_c—are tuned simultaneously to achieve the highest possible gain at ω_n while satisfying the open-loop phase margin requirements. Although a larger gain M is desirable to enhance damping performance, it broadens the crossover frequency range, thus reducing the achievable phase margins. In contrast, increasing the damping coefficient ζ_c improves stability and robustness, but results in a lower controller gain within the primary region of interest. This inherent trade-off necessitates the concurrent tuning of M and ζ_c, which can be effectively optimized using a well-formulated optimization algorithm.

2.7. Effect of controller slope order on stability margins

As clearly illustrated in Figs. 3 and 5, an increase in the controller slope order n results in reduced phase margins $\phi_{1,2}$ at the corresponding crossover frequencies $\omega_{c_{1,2}}$. This decay in phase margin is a consistent trend that persists as the controller slope order continues to increase. The phenomenon is formally characterized and proven in the following proposition.

Proposition 1. *Consider the second-order plant*

$$G(s) = \frac{\omega_n^2}{s^2 + 2\zeta_n\omega_n s + \omega_n^2}$$

and the tunable band-pass controller

$$C_d(s) = g(n)\left(\frac{s}{(s+\omega_n)^2}\right)^n \cdot h(m)(s+\omega_n)^m\,\sigma\left(\frac{s-\omega_d}{s+\omega_d}\right),$$

where $g(n) = M(2\omega_n)^n$ *and* $h(m) = 2^{-m/2}\omega_n^{-m}$.

Let $\mathcal{L}(s) = G(s)e^{-\tau s}C_d(s)$ *be the open loop. Assume that* $\omega_n, \omega_d, \zeta_n > 0$, $M > 2\zeta_n$, $\tau \geq 0$, $m \in \mathbb{Z}_{\geq 0}$, *and* $\sigma \in \{-1, 1\}$ *are fixed, while* $n \in \mathbb{R}_{>0}$ *varies with* $n \geq m$. *Define* $\alpha = M/(2\zeta_n) > 1$ *and* $a = \sqrt{2\ln\alpha} > 0$. *Then there exists an order* N, *depending on the fixed parameters, such that for every* $n > N$:

(i) $\mathcal{L}(s)$ *has exactly two positive unity-gain crossover frequencies* $\omega_{c1} < \omega_n < \omega_{c2}$, *and both are simple;*

(ii) using a continuous phase branch fixed at ω_n, *the signed phase margins*

$$\phi_1(n) = \pi - \arg\mathcal{L}(j\omega_{c1}),$$
$$\phi_2(n) = \pi + \arg\mathcal{L}(j\omega_{c2})$$

satisfy

$$\frac{d\phi_i}{dn} = -\sqrt{\frac{\ln\alpha}{2n}} + O(n^{-3/2}) < 0, \qquad i = 1, 2;$$

(iii) $\phi_1(n) + \phi_2(n) = 2\pi - 2a\sqrt{n} + O(n^{-1/2}) \to -\infty$.

Proof. A complete derivation and proof are provided in Appendix A. □

Proposition 1 shows that the controller slope order cannot be increased indefinitely ($n \to \infty$) in pursuit of steeper magnitude slopes while preserving prescribed positive phase margins under fixed tuning. Part (iii) is independent of the phase branch, of the NMP sign σ, and of the delay. The stability conditions in Eq. (8) imply $\arg\mathcal{L}(j\omega_{c1}) - \arg\mathcal{L}(j\omega_{c2}) \leq 2\pi$ for any integer k; therefore they cannot hold once $2a\sqrt{n}$ exceeds 2π by more than the remainder. This limitation is fundamentally inherent to linear control systems and arises from the Bode gain–phase relationship. The result is asymptotic: monotonic decrease at every finite order is not guaranteed for the complete controller, and the order beyond which it holds grows as the plant damping decreases.

Remark 5. The continuous-order formulation also permits non-integer values of n. Such controllers can be implemented approximately using finite-dimensional rational models over a prescribed frequency band, for example, through fractional-order approximation tools in the CRONE toolbox or by fitting the desired complex frequency response using MATLAB's `tfest`. The approximation band should include the targeted resonance and relevant crossover frequencies, and closed-loop stability and robustness must be verified for the resulting implementation.

3. Illustrative case studies

This section presents three illustrative case studies to evaluate different aspects of the proposed band-pass damping framework. First, a numerical study with closely spaced modes is considered to systematically investigate the influence of controller order on modal selectivity and the preservation of an untargeted neighboring resonance. Subsequently, a collocated nanopositioning system is considered for an experimental closed-loop evaluation of the proposed controller. Finally, a non-collocated flexible-beam system is investigated through closed-loop simulations based on experimentally obtained plant frequency-response data. The latter two case studies demonstrate narrow-band damping of a targeted structural mode while assessing the associated spillover and noise-transmission characteristics. For these cases, the performance of the proposed NBP controllers is compared with benchmark Positive Position Feedback (PPF) and Negative Position Feedback (NPF) controllers.

3.1. Modal selectivity for closely spaced resonances

This numerical study uses a normalized two-mode mechanical model with delay to isolate the effects of controller order and modal spacing on modal selectivity. The system considered is represented as

$$G(s) = \frac{e^{-\tau s}}{2}\sum_{k=1}^{2}\frac{\omega_k^2}{s^2 + 2\zeta_k\omega_k s + \omega_k^2}, \quad \omega_2 = \rho\omega_1 \tag{21}$$

where ζ_k is the damping ratio of mode k, ρ determines the modal spacing, and the delay is approximated using a first-order Padé approximation. The modal damping ratios are adjusted to give equal uncontrolled resonance peak magnitudes. The plant and controller parameters are provided in Appendix B.1.

The first mode is selected as the targeted resonance, while the preservation of the second, untargeted mode is evaluated for different NBP orders. For each plant configuration, the controller gain, corner frequency, and NMP filter parameters are kept fixed, such that the controller order n is the only varying design parameter. Consequently, all controller orders yield the same value of $\mathcal{PS}_{xd}(s)$ at the targeted resonance frequency. Owing to the close proximity of the two resonances, the resulting open-loop responses exhibit four unity-gain crossover frequencies, with two crossovers associated with each resonance. To ensure a consistent comparison under identical stability and robustness requirements, the controllers are designed such that the phase margin at every gain-crossover frequency satisfies $\phi_i \geq 60°$, $i \in 1, 2, 3, 4$.

Here, spillover denotes the unintended modification of the untargeted resonance induced by the damping controller. From the perspective of modal selectivity, both amplification and attenuation represent a deviation from the response intended to be preserved. This distinction is particularly relevant when the untargeted mode serves a specific operational or sensing function, as encountered in resonant piezoelectric motors and bimodal AFM.

Spillover is quantified by the absolute percentage change in the untargeted resonance peak, $\Delta = 100\left|\frac{\max_{\Omega_u}|\mathcal{PS}xd|}{\max\Omega_u|G|} - 1\right|$, where both frequency responses are evaluated at $s = j\omega$ and the maxima are determined over the untargeted-mode interval Ω_u specified in the Appendix B.1. The two maxima are identified independently to account for possible shifts in the resonance frequency. Accordingly, a smaller Δ indicates better preservation of the untargeted resonance.

As a complementary metric, the band-limited $\mathcal{H}_2$ norm of $\mathcal{PS}_{xd}(s)$ is evaluated to distinguish modal selectivity from aggregate vibration reduction. Its signed percentage change relative to the corresponding norm of $G(s)$, denoted by Δ_{H_2}, quantifies the change in the overall response over the considered frequency band, with negative values indicating a reduction. Consequently, attenuation of the untargeted resonance may improve Δ_{H_2} while simultaneously increasing Δ, highlighting the distinction between overall vibration reduction and preservation of an untargeted mode.

Fig. 8 and Table 1 show that increasing n progressively reduces spillover in terms of modification of the untargeted resonance peak, thereby demonstrating improved modal selectivity. However, lower controller orders exhibit greater aggregate vibration reduction. For closely spaced modes, the closed-loop response in the vicinity of the resonances is governed by the combined gain and phase characteristics of the controller, resulting in stronger interaction between the targeted and untargeted modes. In contrast, for well-separated modes, the increasingly steep gain roll-off of the NBP controller with increasing order

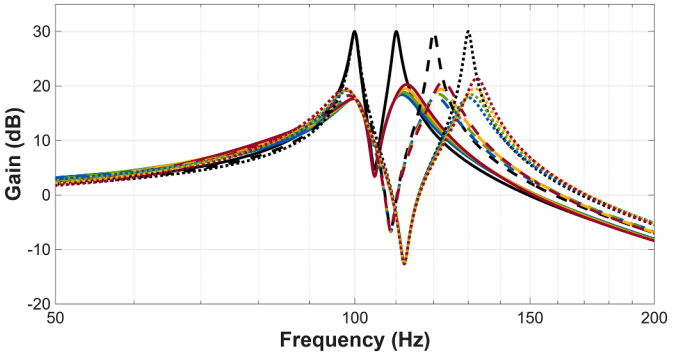


Fig. 8. Simulated frequency response of system $|G(s)|$ (—) and closed-loop $|\mathcal{P}S_{xd}(s)|$ for targeting first-mode suppression via NBP controllers with order: $n = 1$ (—), $n = 2$ (—), $n = 3$ (—), $n = 4$ (—). Solid, dashed, and dotted lines denote $\rho = 1.1$, 1.2, and 1.3, respectively.

Table 1
Quantification of closed-loop spillover Δ and $\mathcal{H}_2$ norm change for variations in controller order n and modal spacing ρ.

ρ	$n = 1$	$n = 2$	$n = 3$	$n = 4$
Absolute untargeted peak change, Δ (%)				
1.1	73.67	72.22	70.19	67.35
1.2	75.15	73.45	70.48	65.57
1.3	75.34	73.72	70.02	62.97
Band-limited $\mathcal{H}_2$ norm change, $\Delta_{\mathcal{H}_2}$ (%)				
1.1	−46.93	−45.10	−43.04	−40.68
1.2	−46.93	−45.03	−42.61	−39.45
1.3	−45.59	−43.74	−41.03	−37.02

substantially reduces its influence at the untargeted resonance, making the corresponding phase interaction less significant.

Although these observations are specific to the configurations investigated here, future analytical and numerical studies will examine the influence of collocation, pole–zero structure, minimum- and nonminimum-phase dynamics, and modal spacing to establish more general tuning and design guidelines.

3.2. Noise attenuation in collocated nanopositioning stage

The system considered in this study is a P-621.1CD PIHera nanopositioning platform, as shown in Fig. 9, on which the proposed controllers are experimentally implemented. The setup comprises a piezoelectric stack actuator driving a flexure-guided stage with a travel range of 100 μm and an integrated capacitive sensor in a collocated configuration. A PI E-712 unit provides the drive amplifier and sensor conditioning, interfaced with an NI CompactRIO FPGA through 16-bit analog input–output modules with a 0–10 V command range. The controllers are discretized using the Tustin transform and implemented in LabVIEW with a sampling period of 30 μs (33.33 kHz).

For system identification, a sinusoidal chirp ranging from 0.75 to 1 V is applied to the amplifier command input, and the capacitive-sensor output is recorded. The input–output data are processed using the MATLAB Signal Processing Toolbox to estimate the plant frequency response up to 3000 Hz. As shown in Fig. 10, the measured plant response exhibits a dominant resonance at 782 Hz and additional higher-order resonances. The observed pole–zero interlacing is consistent with the collocated configuration. Additional phase lag is present due to the actuator-amplifier dynamics and effective system delay.

For reproducibility, an analytical model is constructed from a dominant second-order mode, two additional resonance–antiresonance pairs, a first-order electrical roll-off, a first-order lead–lag factor, and an explicit delay. The parameters are manually adjusted by comparing the model magnitude and phase with the measured frequency response over 10–3000 Hz. The resulting model has the form

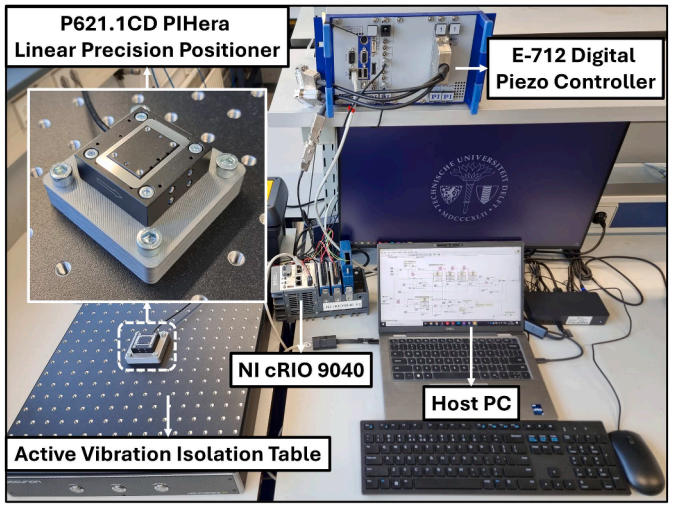


Fig. 9. Experimental setup with a P-621.1CD PIHera piezo-actuated nanopositioning system.

$$G_{\text{fit}}(s) = \frac{\sum_{i=0}^{5} b_i s^i}{\sum_{j=0}^{8} a_j s^j} e^{-\tau s}, \qquad a_8 = 1, \tag{22}$$

with an effective delay of $\tau = 230\,\mu$s. The polynomial coefficients are provided in Appendix B.2. The model supports reproducibility of the frequency-domain analysis, while the controller comparisons in this case study are evaluated experimentally.

In such systems, the first dominant resonance typically limits control bandwidth and stability margins. To address this, the proposed band-pass damping controller is implemented to suppress this mode at 782 Hz. Two controller configurations with slope orders $n = 1$ and $n = 2$ are evaluated to examine the influence of steeper magnitude slopes on damping performance. For a fair comparison, the PPF and NPF controllers are designed to achieve the same level of damping ($\approx$ 21.3 dB reduction) at the targeted resonance as the proposed band-pass controllers. Since the system exhibits inherent delay, all damping controllers are delay-compensated using the NMP filter introduced in Section 2.5, consistent with the generalized delay-compensation framework (Natu & HosseinNia, 2026b). As shown in Fig. 10(a), the closed-loop response of $\mathcal{P}S_{xd}(s)$ at the targeted resonance shows minimal variation, while the NPF controller, lacking gain roll-off, amplifies the second resonance in the vicinity.

The key distinction among the controllers appears in the noise attenuation performance, represented by the magnitude of the closed-loop function $S_{xn}(s)$ (see Fig. 10(b)). The PPF controller exhibits high noise transmission at low frequencies due to its low-pass characteristics and constant gain in this region. Conversely, the NPF controller maintains constant gain at high frequencies, leading to amplified noise transmission in that range. As discussed in Section 1, band-pass control is employed to mitigate such low- and high-frequency noise transmission relative to the targeted resonance mode. For the band-pass controller with slope order $n = 1$, providing $\pm$20 dB/decade slopes around the resonance, the noise transmission is reduced at low and high frequencies compared with the PPF and NPF controllers, respectively. Increasing the order to $n = 2$ yields $\pm$40 dB/decade slopes and provides a steeper gain roll-off on both sides of the targeted resonance.

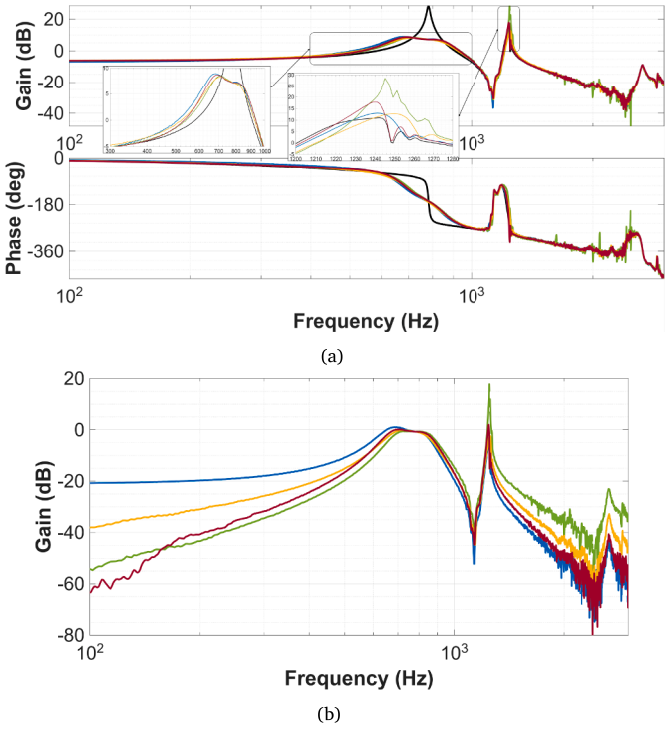


Fig. 10. Experimental frequency response of collocated nanopositioning system $G(s)$ (—) and closed-loop response obtained via implementing active damping controller $C_d(s)$ as PPF controller (—), NPF controller (—), proposed band-pass controller with $n = 1$ (—), and with $n = 2$ (—). (a) $\mathcal{P}S_{xd}(s)$, (b) $|S_{xn}(s)|$.

Table 2
Experimental noise-transmission metrics obtained from closed-loop $S_{xn}(s)$.All metrics are reported in $\mathrm{m}\sqrt{\mathrm{Hz}}/\mathrm{V}$.

Controller	$\|S_{xn}\|_{\mathcal{H}_2}$	J_L	J_H	J_{OOB}
PPF	16.72	3.185	0.196	3.191
NPF	23.93	0.771	1.134	1.371
NBP ($n = 1$)	15.03	1.532	0.464	1.601
NBP ($n = 2$)	15.96	1.101	0.271	1.133

To quantify these observations, the band-limited $\mathcal{H}_2$ norm of S_{xn} is evaluated over 1–3000 Hz. In addition, the low- and high-frequency noise-transmission metrics are defined as

$$J_k = \sqrt{\int_{\mathcal{F}_k} \left|S_{xn}(j2\pi f)\right|^2 df}, \qquad k \in \{L, H\}, \tag{23}$$

where $\mathcal{F}_L = [1, 500]$ Hz and $\mathcal{F}_H = [1500, 3000]$ Hz are selected away from the principal resonance region in which the damping controllers actively shape the closed-loop response. The aggregate out-of-band noise transmission is subsequently quantified as

$$J_{\mathrm{OOB}} = \sqrt{J_L^2 + J_H^2}. \tag{24}$$

Accordingly, smaller values of J_L, J_H, and J_{OOB} indicate lower noise transmission over the corresponding frequency regions.

The experimentally obtained metrics are summarized in Table 2. The PPF exhibits the lowest high-frequency noise transmission, consistent with its high-frequency roll-off, but performs poorly in the low-frequency region due to its low-pass gain characteristics. Conversely, the NPF provides the lowest low-frequency noise transmission at the expense of increased transmission at high frequencies. The NBP controllers provide gain roll-off on both sides of the targeted resonance, thereby offering a more balanced out-of-band response. In particular, increasing the NBP order from $n = 1$ to $n = 2$ reduces J_L and J_H by approximately 28% and 42%, respectively, resulting in an approximately 29% reduction in the aggregate out-of-band metric J_{OOB}. The $n = 2$ NBP consequently achieves the lowest J_{OOB} among the considered controllers. It should be noted that the PPF and $n = 2$ NBP exhibit the same asymptotic high-frequency roll-off slope, while the NPF and $n = 2$ NBP exhibit the same asymptotic low-frequency roll-off slope. The corresponding noise-transmission levels nevertheless differ because $S_{xn}(s)$ is determined by both the controller gain and its closed-loop interaction with the plant over the respective frequency intervals, rather than by the asymptotic slope alone.

Interestingly, the complete band-limited $\mathcal{H}_2$ norm is slightly lower for the $n = 1$ NBP than for the $n = 2$ case. This metric also includes the resonant region, where the controllers are tuned to provide comparable damping at the targeted mode, and the resulting noise response is influenced by the local closed-loop peaks, phase interaction, NMP-filter tuning, and spillover around the untargeted resonance. These contributions can dominate the complete-band integral despite improved attenuation away from the resonances. This is consistent with the fundamental loop-shaping trade-off discussed in Section 2: increased damping around the controlled resonance can be accompanied by increased noise transmission in its vicinity. Hence, the complete $\mathcal{H}_2$ norm characterizes the overall noise performance, whereas J_L, J_H, and J_{OOB} specifically quantify the out-of-band attenuation associated with the controller roll-off.

3.3. Spillover reduction in non-collocated flexural beam

The system considered in this case study is a flexural cantilever beam with base excitation and tip acceleration measurement, adapted from Kaczmarek and HosseinNia (2024). The aluminium-alloy beam has a free length of 410 mm and a thickness of 2 mm; the reference study assumes a density of $2700\,\mathrm{kg\,m^{-3}}$ and Young's modulus of 69 GPa. Its base is clamped to a Brüel & Kjær Type 4809 vibration shaker driven by a Type 2706 amplifier, while the opposite end remains free. Two Brüel & Kjær Type 4508 B accelerometers measure the base and tip accelerations. The experimental platform uses an NI cRIO-9039 FPGA system operating at 10 kHz, with an NI 9264 module generating the excitation signal and an NI 9234 module acquiring the accelerometer signals.

The uncontrolled frequency response is obtained using a frequency-sweep excitation. The measured base and tip accelerations define the acceleration transmissibility, which is used as the plant response $G(s)$ in this study. Base excitation and tip sensing form a non-collocated input–output configuration, whose measured response contains multiple lightly damped resonances. The proposed damping controllers are evaluated through closed-loop simulations using this experimentally identified response, as shown in Fig. 11. Such flexible structures are highly sensitive to external disturbances, where resonance excitation can result in large vibration amplitudes.

For reproducibility, the measured complex frequency response over 2–600 Hz is approximated by a continuous-time rational transfer function with an explicit delay,

$$G_{\mathrm{fit}}(s) = \frac{\sum_{i=0}^{14} b_i s^i}{\sum_{j=0}^{16} a_j s^j} e^{-\tau s}, \qquad a_{16} = 1, \tag{25}$$

where the rational part contains 16 poles and 14 zeros, and the effective delay is $\tau = 2.52$ ms. The model parameters are adjusted to reproduce the measured magnitude and phase. The polynomial coefficients are provided in Appendix B.3.

Similar to the previous case, four controllers are evaluated to induce an equivalent amount of damping at the second non-collocated mode at 53.7 Hz. As observed, the PPF controller exhibits the highest spillover before the targeted resonance due to its low-pass characteristics, although its −40 dB/decade roll-off beyond resonance effectively

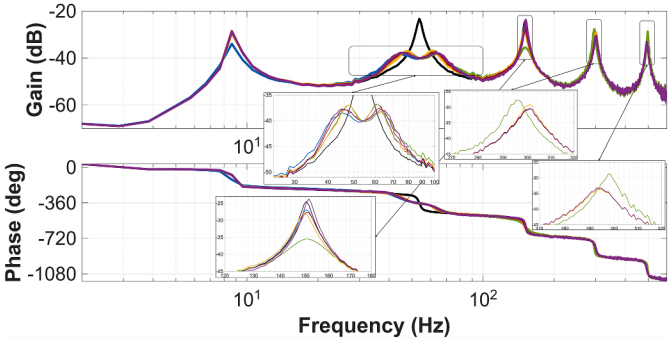


Fig. 11. Simulated frequency response of non-collocated flexural beam $G(s)$ (—) and closed-loop response $\mathcal{PS}_{xd}(s)$ obtained via implementing active damping controller $C_d(s)$ as PPF controller (—), NPF controller (—), proposed band-pass controller with $n = 1$ (—), $n = 2$ (—), and $n = 4$ (—).

Table 3
Targeted-mode phase margins and absolute magnitude differences at untargeted resonances for equal attenuation at resonance. Frequencies in $\Delta(f)$ are expressed in Hz.

Controller	ϕ_1 (°)	ϕ_2 (°)	$\Delta(8.63)$ (dB)	$\Delta(150.52)$ (dB)	$\Delta(301.04)$ (dB)	$\Delta(492.79)$ (dB)
PPF	61.09	60.91	5.247	2.447	0.029	0.028
NPF	60.91	60.86	0.046	10.995	3.045	0.836
NBP, $n = 1$	60.84	60.80	1.033	3.681	1.268	0.443
NBP, $n = 2$	60.51	60.49	0.188	3.147	0.026	0.047
NBP, $n = 4$	60.61	60.56	0.119	0.264	0.125	0.002

prevents excitation of higher-order modes. In contrast, the NPF controller yields minimal pre-resonance spillover but significantly amplifies the fourth and fifth modes at higher frequencies due to its constant high-frequency gain.

The band-pass controller with slope order $n = 1$, providing ± 20 dB/decade slopes around the resonance, achieves reduced spillover near the targeted mode and noticeably less amplification of the fourth mode, with minimal effect on the fifth. This behavior arises because the -20 dB/decade roll-off is sufficient to not influence the fifth mode but not the fourth, given their relative frequency spacing. To improve attenuation, two narrow band-pass controllers with slope orders $n = 2$ and $n = 4$ are implemented, providing steeper ± 40 and ± 80 dB/decade slopes, respectively, that effectively eliminate amplification of the higher-order modes. However, as also noted in the previous subsection, the increased slope order reduces phase margins at the crossover frequencies, leading to a slightly higher response amplitude around the targeted resonance compared to the $n = 1$ case. This again demonstrates the fundamental trade-off between slope sharpness and phase robustness in linear control systems.

For equal attenuation at the targeted resonance of 53.7 Hz, Table 3 compares the two crossover phase margins and the absolute magnitude difference in dB, defined as $\Delta(f) = \left|20\log_{10}|\mathcal{PS}_{xd}(j2\pi f)| - 20\log_{10}|G(j2\pi f)|\right|$, at the untargeted resonances. With all margins slightly above 60°, increasing n from 1 to 2 reduces all four differences. Increasing n to 4 further reduces the three differences significantly, particularly at 150.52 and 492.79 Hz, although the difference at 301.04 Hz is marginally increased due to open-loop phase interaction.

4. Conclusion

This paper presents a generalized higher-order band-pass active damping framework for improving modal selectivity and stability in lightly damped mechatronic and structural systems. The proposed tunable band-pass controller, formulated within the loop-shaping paradigm, enables narrow-band damping around the targeted resonance while maintaining low gain elsewhere. Analytical results establish explicit relationships between controller order, slope characteristics, and phase margins, offering systematic design guidelines. The inclusion of a non-minimum-phase filter compensates for delay-induced phase lag, while a tunable damping coefficient enhances flexibility in shaping closed-loop dynamics. Experimental results from a nanopositioning stage with collocated actuation and sensing demonstrate improved out-of-band noise attenuation at comparable targeted resonance suppression. Closed-loop simulations using an experimentally identified non-collocated beam response demonstrate reduced spillover in the investigated configuration. A separate numerical study of closely spaced resonances shows that improved preservation of an untargeted peak need not coincide with greater aggregate vibration reduction. These findings support selecting the controller order according to modal-selectivity, noise-transmission, and robustness requirements. Future work will examine the influence of actuator–sensor configuration, pole–zero structure, delay, and modal spacing to develop broader design guidelines.

CRediT authorship contribution statement

Aditya Natu: Writing – review & editing, Writing – original draft, Visualization, Validation, Software, Project administration, Methodology, Investigation, Formal analysis, Data curation, Conceptualization; **Hassan HosseinNia:** Writing – review & editing, Validation, Supervision, Resources, Methodology, Investigation, Funding acquisition, Formal analysis, Conceptualization.

Declaration of competing interest

The authors declare that they have no known competing financial interests or personal relationships that could have appeared to influence the work reported in this paper.

Acknowledgments

This work was financed by Physik Instrumente (PI) SE & Co. KG and co-financed by Holland High Tech with PPS Project supplement for research and development in the field of High Tech Systems and Materials.

The authors express their sincere gratitude to both Mathias Winter, Head of Piezo System & Drive Technology, and Dr.-Ing. Simon Kapelke, Head of Piezo Fundamental Technology, from Physik Instrumente (PI) SE & Co. KG, for their invaluable collaboration in providing technical insights concerning the system and its applications.

Data availability

Data will be made available on request.

Appendix A. Proof of Proposition 1

All parameters other than n are held fixed. Since $n \geq m \geq 0$ and $n > 0$,

$$n - \frac{m}{2} \geq \frac{n}{2} > 0. \tag{A.1}$$

Step 1: Normalization and open-loop magnitude. Introduce

$$x = \frac{\omega}{\omega_n}, \qquad \delta = \tau\omega_n,$$
$$r = \frac{\omega_d}{\omega_n}, \qquad \alpha = \frac{M}{2\zeta_n} > 1, \tag{A.2}$$

and

$$D(x) = (1 - x^2)^2 + 4\zeta_n^2 x^2. \tag{A.3}$$

The delay and the NMP filter have unit magnitude, hence

$$\left|\mathcal{L}(j\omega_n x)\right| = \frac{M}{\sqrt{D(x)}}\left(\frac{2x}{1+x^2}\right)^n\left(\frac{1+x^2}{2}\right)^{m/2}. \tag{A.4}$$

Define

$$\begin{aligned}\lambda(x) &= \ln\left(\frac{2x}{1+x^2}\right),\\ \mu(x) &= \frac{1}{2}\ln\left(\frac{1+x^2}{2}\right),\end{aligned} \tag{A.5}$$

so that $\lambda(x) < 0$ for $x \neq 1$ and $\lambda(1) = \mu(1) = 0$. The logarithmic magnitude is

$$\begin{aligned}A(x,n) &:= \ln\left|\mathcal{L}(j\omega_n x)\right|\\ &= \ln M - \frac{1}{2}\ln D(x) + n\lambda(x) + m\mu(x).\end{aligned} \tag{A.6}$$

At the targeted frequency, $A(1,n) = \ln\alpha > 0$ for every n. For fixed n,

$$\left|\mathcal{L}(j\omega_n x)\right| \sim \begin{cases} M\,2^{n-m/2}\,x^n, & x \to 0^+,\\ M\,2^{n-m/2}\,x^{m-n-2}, & x \to \infty.\end{cases} \tag{A.7}$$

Because $n > 0$ and $n \geq m$ (so $n > m-2$), the magnitude tends to zero at both endpoints. Thus, at least one unity-gain crossover exists on each side of $x = 1$. Uniqueness and simplicity for sufficiently large n are established in Step 4.

Step 2: Continuous phase. Define

$$\begin{aligned}\Phi(x,n) &:= \arg\mathcal{L}(j\omega_n x)\\ &= \theta(x) + n\psi(x) + m\arctan x + q_\sigma(x) - \delta x,\end{aligned} \tag{A.8}$$

with

$$\begin{aligned}\theta(x) &= -\operatorname{atan2}(2\zeta_n x,\ 1-x^2),\\ \psi(x) &= \frac{\pi}{2} - 2\arctan x,\\ q_\sigma(x) &= \pi - 2\arctan(x/r) + \chi_\sigma,\end{aligned} \tag{A.9}$$

where $\chi_{+1} = 0$ and $\chi_{-1} = -\pi$. Fractional powers are taken with the continuous phase of their base factors ($\psi \in (-\pi/2, \pi/2)$ and $\arctan x \in (0, \pi/2)$), so Φ is smooth in (x,n). At $x = 1$,

$$\Phi(1,n) = \Phi_0 := -\frac{\pi}{2} + \frac{m\pi}{4} + q_\sigma(1) - \delta, \tag{A.10}$$

which is independent of n (since $\psi(1) = 0$). This fixes the phase branch. Adding a constant multiple of 2π to Φ changes none of the derivatives below.

Step 3: Exact finite-order sensitivity. Differentiating (A.6) and (A.8),

$$\begin{aligned}A_x(x,n) &= \frac{2x(1-x^2-2\zeta_n^2)}{D(x)}\\ &\quad + n\frac{1-x^2}{x(1+x^2)} + \frac{mx}{1+x^2},\\ A_n(x,n) &= \lambda(x),\end{aligned} \tag{A.11}$$

$$\begin{aligned}\Phi_x(x,n) &= -\frac{2\zeta_n(1+x^2)}{D(x)} + \frac{m-2n}{1+x^2}\\ &\quad - \frac{2r}{r^2+x^2} - \delta,\\ \Phi_n(x,n) &= \psi(x).\end{aligned} \tag{A.12}$$

Consider simple crossover branches $x_{c1}(n) < 1 < x_{c2}(n)$ satisfying

$$A(x_{ci}(n), n) = 0, \qquad i = 1,2, \tag{A.13}$$

with crossing directions

$$A_x(x_{c1}, n) > 0, \qquad A_x(x_{c2}, n) < 0. \tag{A.14}$$

Implicit differentiation gives

$$\frac{dx_{ci}}{dn} = -\frac{\lambda(x_{ci})}{A_x(x_{ci}, n)}. \tag{A.15}$$

Since $\lambda(x) < 0$ for $x \neq 1$, the crossing directions in (A.14) imply

$$\frac{dx_{c1}}{dn} > 0, \qquad \frac{dx_{c2}}{dn} < 0, \tag{A.16}$$

i.e., both crossovers move toward the targeted frequency as n increases. Along a crossover branch, the total phase derivative satisfies

$$\begin{aligned}\frac{d}{dn}\Phi(x_{ci}(n), n) &= \Phi_n(x_{ci}, n) + \Phi_x(x_{ci}, n)\frac{dx_{ci}}{dn}\\ &= \psi(x_{ci}) - \frac{\Phi_x(x_{ci}, n)\lambda(x_{ci})}{A_x(x_{ci}, n)}.\end{aligned} \tag{A.17}$$

With $\phi_1 = \pi - \Phi(x_{c1}, n)$ and $\phi_2 = \pi + \Phi(x_{c2}, n)$,

$$\begin{aligned}\frac{d\phi_1}{dn} &= -\psi(x_{c1}) + \frac{\Phi_x(x_{c1}, n)\lambda(x_{c1})}{A_x(x_{c1}, n)},\\ \frac{d\phi_2}{dn} &= \psi(x_{c2}) - \frac{\Phi_x(x_{c2}, n)\lambda(x_{c2})}{A_x(x_{c2}, n)}.\end{aligned} \tag{A.18}$$

Under (A.14), both margins decrease at a given order if and only if

$$\psi(x_{ci})A_x(x_{ci}, n) - \Phi_x(x_{ci}, n)\lambda(x_{ci}) > 0 \tag{A.19}$$

holds at both $i = 1$ and $i = 2$. This is the exact finite-order monotonicity condition for the complete controller. It is not implied by the phase advance of the NMP filter, as the following decomposition shows. Let $\phi_i^{(m)}$ denote the margins of the same m-modified controller without the NMP filter and delay. Since these factors have unit magnitude, the crossover frequencies remain unchanged and

$$\begin{aligned}\phi_1 &= \phi_1^{(m)} - q_\sigma(x_{c1}) + \delta x_{c1},\\ \phi_2 &= \phi_2^{(m)} + q_\sigma(x_{c2}) - \delta x_{c2}.\end{aligned} \tag{A.20}$$

Differentiating gives

$$\begin{aligned}\frac{d\phi_1}{dn} &= \frac{d\phi_1^{(m)}}{dn} + \left(\frac{2r}{r^2+x_{c1}^2} + \delta\right)\frac{dx_{c1}}{dn},\\ \frac{d\phi_2}{dn} &= \frac{d\phi_2^{(m)}}{dn} - \left(\frac{2r}{r^2+x_{c2}^2} + \delta\right)\frac{dx_{c2}}{dn}.\end{aligned} \tag{A.21}$$

Both corrections are positive by (A.16): the NMP filter and the delay slow the decrease of the margins with n and may even reverse it at low order. These corrections concern the variation of the margins with n, rather than an improvement in both margin values. Accordingly, monotonic decrease at every finite order requires verification of (A.19). The remainder of the proof establishes that both margins nevertheless decrease strictly for all sufficiently large n.

Step 4: Exactly two simple crossovers for large n. Introduce $t = \ln x$ and $\hat{A}(t,n) = A(e^t, n)$. Using

$$\begin{aligned}\frac{2x}{1+x^2} &= \frac{1}{\cosh t}, \qquad \frac{1+x^2}{2} = e^t\cosh t,\\ D(e^t) &= 4e^{2t}(\sinh^2 t + \zeta_n^2),\end{aligned}$$

the logarithmic magnitude becomes

$$\hat{A}(t,n) = \ln\alpha + bt - \left(n - \frac{m}{2}\right)\ln\cosh t - \kappa(t), \tag{A.22}$$

where

$$b = \frac{m}{2} - 1, \qquad \kappa(t) = \frac{1}{2}\ln\left(1 + \frac{\sinh^2 t}{\zeta_n^2}\right) \geq 0. \tag{A.23}$$

Fix any $\eta > 0$. For $|t| \geq \eta$, since $\kappa \geq 0$ and by (A.1),

$$\begin{aligned}\hat{A}(t,n) &\leq \ln\alpha + |b||t| - \frac{n}{2}\ln\cosh t\\ &= \ln\cosh t\left(\frac{\ln\alpha + |b||t|}{\ln\cosh t} - \frac{n}{2}\right).\end{aligned} \tag{A.24}$$

The ratio $(\ln\alpha + |b||t|)/\ln\cosh t$ is continuous on $|t| \geq \eta$ and has a finite limit as $|t| \to \infty$; hence it is bounded by some constant K_η. Thus $\hat{A}(t,n) < 0$ for all $|t| \geq \eta$ once $n > 2K_\eta$, and every crossover lies in $(-\eta, \eta)$.

On $[-\eta,\eta]$, the function κ'' is bounded, whereas $\operatorname{sech}^2 t \geq \operatorname{sech}^2 \eta > 0$. By (A.1),

$$\begin{aligned}\hat{A}_{tt}(t,n) &= -\left(n-\frac{m}{2}\right)\operatorname{sech}^2 t - \kappa''(t)\\ &\leq -\frac{n}{2}\operatorname{sech}^2\eta - \max_{[-\eta,\eta]}\left|\kappa''\right| < 0\end{aligned} \tag{A.25}$$

for all sufficiently large n. Since $\hat{A}(0,n) = \ln\alpha > 0$ and $\hat{A}(\pm\eta,n) < 0$, strict concavity gives exactly two roots $t_{c1} < 0 < t_{c2}$, with

$$\hat{A}_t(t_{c1},n) > 0, \qquad \hat{A}_t(t_{c2},n) < 0. \tag{A.26}$$

Since $\hat{A}_t = xA_x$, these roots also satisfy (A.14). This establishes part (i) of the proposition: existence, uniqueness, and simplicity of the crossovers at sufficiently large order.

Step 5: Crossover locations. Near $t = 0$,

$$\begin{aligned}\ln\cosh t &= \frac{t^2}{2} - \frac{t^4}{12} + O(t^6),\\ \kappa(t) &= \frac{t^2}{2\zeta_n^2} + O(t^4).\end{aligned} \tag{A.27}$$

Substitution into (A.22) gives

$$\begin{aligned}\hat{A}(t,n) &= \ln\alpha + bt - \frac{nt^2}{2}\\ &\quad + \left(\frac{m}{4} - \frac{1}{2\zeta_n^2}\right)t^2 + \frac{nt^4}{12} + O(t^4) + O(nt^6).\end{aligned} \tag{A.28}$$

The leading balance suggests $t = O(n^{-1/2})$. Set $\varepsilon = n^{-1/2}$ and $t = \varepsilon y$. For bounded y,

$$\hat{A}(\varepsilon y, \varepsilon^{-2}) = \ln\alpha - \frac{y^2}{2} + b\varepsilon y + O(\varepsilon^2). \tag{A.29}$$

After removal of the singularity at $\varepsilon = 0$, this expression is analytic in (y,ε). Its limiting roots are $y = \pm a$, and the derivative with respect to y, namely $\mp a$, is nonzero at both roots. The analytic implicit-function theorem therefore provides analytic root branches $y_i(\varepsilon)$. Writing $y = y_0 + c\varepsilon + O(\varepsilon^2)$ with $y_0 = \pm a$, the coefficient of ε in (A.29) gives $-y_0 c + by_0 = 0$. Thus $c = b$, and

$$\begin{aligned}t_{c1} &= -a\,n^{-1/2} + b\,n^{-1} + O(n^{-3/2}),\\ t_{c2} &= a\,n^{-1/2} + b\,n^{-1} + O(n^{-3/2}).\end{aligned} \tag{A.30}$$

In ordinary normalized frequency, $x_{ci} = e^{t_{ci}}$, so

$$\begin{aligned}x_{c1} &= 1 - \frac{a}{\sqrt{n}} + \frac{b + a^2/2}{n} + O(n^{-3/2}),\\ x_{c2} &= 1 + \frac{a}{\sqrt{n}} + \frac{b + a^2/2}{n} + O(n^{-3/2}).\end{aligned} \tag{A.31}$$

The crossover separation therefore decreases proportionally to $n^{-1/2}$.

Step 6: Phase at the crossovers and margin asymptotics. Define $\hat{\Phi}(t,n) = \Phi(e^t,n)$. The identities

$$\begin{aligned}\theta(e^t) &= -\frac{\pi}{2} - \arctan\left(\frac{\sinh t}{\zeta_n}\right),\\ \psi(e^t) &= -\arctan(\sinh t),\\ \arctan(e^t) &= \frac{\pi}{4} + \frac{1}{2}\arctan(\sinh t)\end{aligned} \tag{A.32}$$

give the exact expression

$$\begin{aligned}\hat{\Phi}(t,n) &= -\frac{\pi}{2} + \frac{m\pi}{4} - \arctan\left(\frac{\sinh t}{\zeta_n}\right)\\ &\quad - \left(n - \frac{m}{2}\right)\arctan(\sinh t) + q_\sigma(e^t) - \delta e^t.\end{aligned} \tag{A.33}$$

Since $\arctan(\sinh t) = t + O(t^3)$ and the remaining terms are smooth at $t = 0$,

$$\hat{\Phi}(t,n) = \Phi_0 - nt + O(t) + O(nt^3). \tag{A.34}$$

At either crossover, $t_{ci} = O(n^{-1/2})$, so both remainder terms are $O(n^{-1/2})$. Using (A.30),

$$\begin{aligned}\hat{\Phi}(t_{c1},n) &= \Phi_0 - b + a\sqrt{n} + O(n^{-1/2}),\\ \hat{\Phi}(t_{c2},n) &= \Phi_0 - b - a\sqrt{n} + O(n^{-1/2}).\end{aligned} \tag{A.35}$$

The signed margins consequently satisfy

$$\begin{aligned}\phi_1(n) &= \pi - \Phi_0 + b - a\sqrt{n} + O(n^{-1/2}),\\ \phi_2(n) &= \pi + \Phi_0 - b - a\sqrt{n} + O(n^{-1/2}).\end{aligned} \tag{A.36}$$

Because $a = \sqrt{2\ln\alpha} > 0$, both margins tend to $-\infty$. The fixed slope-adjustment term, NMP filter, and delay affect the constant offsets, but not the leading decrease proportional to $\sqrt{n}$.

Subtracting the two expressions in (A.35) cancels Φ_0 and b, and with them every dependence on σ, ω_d, τ, and on the chosen phase branch:

$$\begin{aligned}\arg\mathcal{L}(j\omega_{c1}) - \arg\mathcal{L}(j\omega_{c2}) &= 2a\sqrt{n} + O(n^{-1/2}),\\ \phi_1 + \phi_2 &= 2\pi - 2a\sqrt{n} + O(n^{-1/2}).\end{aligned} \tag{A.37}$$

This establishes part (iii). It also shows that the stability conditions in Eq. (8) cannot hold for large n for any integer k. Adding the two inequalities in Eq. (8) gives

$$\arg\mathcal{L}(j\omega_{c1}) - \arg\mathcal{L}(j\omega_{c2}) \leq 2\pi,$$

which contradicts (A.37) as soon as $2a\sqrt{n}$ exceeds 2π by more than the remainder.

Step 7: Eventual monotonic decrease. Eventual monotonicity requires justification for differentiating the expansions. The analytic crossover branches $t_{ci} = \varepsilon y_i(\varepsilon)$ from Step 5, substituted into (A.33), yield convergent Laurent expansions in ε of the form

$$\phi_i = -\frac{a}{\varepsilon} + c_i + R_i(\varepsilon), \qquad i = 1,2, \tag{A.38}$$

where $c_1 = \pi - \Phi_0 + b$, $c_2 = \pi + \Phi_0 - b$, and R_i is analytic with $R_i(0) = 0$; hence $R_i'(\varepsilon) = O(1)$. Since $d\varepsilon/dn = -\varepsilon^3/2$,

$$\frac{d\phi_i}{dn} = \left(\frac{a}{\varepsilon^2} + R_i'(\varepsilon)\right)\left(-\frac{\varepsilon^3}{2}\right) = -\frac{a}{2\sqrt{n}} + O(n^{-3/2}). \tag{A.39}$$

Therefore,

$$\begin{aligned}\frac{d\phi_1}{dn} &= -\sqrt{\frac{\ln\alpha}{2n}} + O(n^{-3/2}),\\ \frac{d\phi_2}{dn} &= -\sqrt{\frac{\ln\alpha}{2n}} + O(n^{-3/2}).\end{aligned} \tag{A.40}$$

The leading terms are strictly negative and dominate the remainders for sufficiently large n. Choosing N as the largest of the thresholds used in Steps 4–7 proves part (ii). Both margins therefore decrease strictly for all $n > N$, completing the proof. □

Remark 6. The constants hidden in the $O(\cdot)$ terms depend on all fixed parameters. In particular, (A.28) shows that the quadratic coefficient is $-\frac{1}{2}\left(n - \frac{m}{2} + \zeta_n^{-2}\right)$, so the leading balance $\ln\alpha = nt^2/2$ is accurate only for $n \gg \zeta_n^{-2}$. For lightly damped plants, N is therefore expected to be of the order of ζ_n^{-2} or larger. The exact condition (A.19) should be used to assess the finite-order behavior in a design.

Appendix B. Tuned parameters for case studies

B.1. Case study 1: modal selectivity

The damping ratios are computed numerically to match the prescribed resonance peak magnitudes, with rounded values presented here (see Tables B.1, and B.2).

Untargeted peak-search interval Ω_u: $[\sqrt{\omega_1\omega_2}, 10\omega_2]$ (rad/s).

All parameters except n are shared across orders within a plant case.

Table B.1
Plant parameters for case study 1.

Parameter	$\rho = 1.1$	$\rho = 1.2$	$\rho = 1.3$
$\omega_1/(2\pi)$ (Hz)	100	100	100
$\omega_2/(2\pi)$ (Hz)	110	120	130
ζ_1	0.008	0.008	0.008
ζ_2	0.008	0.008	0.008
Delay τ (ms)	1	1	1

Table B.2
Controller parameters for case study 1.

Parameter	$\rho = 1.1$	$\rho = 1.2$	$\rho = 1.3$
n	1, 2, 3, 4	1, 2, 3, 4	1, 2, 3, 4
M	0.1	0.1	0.1
m	0	0	0
ζ_c	0	0	0
$\omega_c/(2\pi)$ (Hz)	100	100	100
$\omega_d/(2\pi)$ (Hz)	171	274	485
σ	+1	+1	+1

Table B.3
Polynomial coefficients of the fitted nanopositioning plant, rounded to four decimal places.

Power i	Numerator b_i	Denominator a_i
8	—	1
7	—	4.0798×10^{4}
6	—	6.6305×10^{8}
5	5.1909×10^{11}	1.4818×10^{13}
4	4.8491×10^{15}	1.2778×10^{17}
3	1.5065×10^{20}	1.0277×10^{21}
2	1.3256×10^{24}	7.2673×10^{24}
1	6.3194×10^{27}	1.6899×10^{28}
0	5.3859×10^{31}	1.0933×10^{32}

B.2. Case study 2: collocated nanopositioning system

The polynomial coefficients of the nanopositioning model in Eq. (22) are listed in Table B.3. The numerator and denominator degrees are $p = 5$ and $q = 8$, respectively, with $a_8 = 1$. The effective delay $\tau = 230\,\mu$s is retained separately from the rational part. The coefficients correspond to $s = j\omega$ with ω expressed in $\mathrm{rad\,s^{-1}}$. A dash denotes a zero numerator coefficient.

The PPF and NPF benchmark controllers use the same negative-feedback convention and are given by

$$C_{\mathrm{PPF}}(s) = -\frac{g\omega_c^2}{s^2 + 2\zeta_c\omega_c s + \omega_c^2}\sigma\frac{s-\omega_d}{s+\omega_d}, \tag{B.1}$$

$$C_{\mathrm{NPF}}(s) = \frac{gs^2}{s^2 + 2\zeta_c\omega_c s + \omega_c^2}\sigma\frac{s-\omega_d}{s+\omega_d}. \tag{B.2}$$

The controller parameters are summarized in Table B.4. All controllers are discretized using the Tustin transform with a sampling period of 30 μs. Dashes indicate parameters that do not apply.

B.3. Case study 3: non-collocated flexible beam

The polynomial coefficients of the fitted beam model in Eq. (25) are listed in Table B.5. The numerator and denominator degrees are 14 and 16, respectively, with $a_{16} = 1$. The effective delay $\tau = 2.52\,\mathrm{ms}$ is retained separately from the rational part. The coefficients correspond to s expressed in $\mathrm{rad\,s^{-1}}$. A dash denotes a zero numerator coefficient. The controller parameters are summarized in Table B.6.

Table B.4
Controller parameters for the nanopositioning case study.

Parameter	PPF	NPF	NBP	NBP
g	0.1989	0.1989	—	—
M	—	—	0.4	0.4
n	—	—	1	2
m	—	—	0	0
ζ_c	0.25	0.25	0.25	0.40
$\omega_c/(2\pi)$ (Hz)	778	778	778	778
ω_d (rad/s)	4200	3900	70000	50000
σ	+1	+1	+1	+1

Table B.5
Polynomial coefficients of the fitted beam model.

Power i	Numerator b_i	Denominator a_i
16	—	1
15	—	-6.797×10^{2}
14	-5.212×10^{3}	3.440×10^{7}
13	-2.304×10^{7}	1.615×10^{9}
12	-1.412×10^{11}	3.968×10^{14}
11	-3.236×10^{14}	1.756×10^{17}
10	-8.892×10^{17}	1.884×10^{21}
9	-1.049×10^{21}	1.224×10^{24}
8	-1.504×10^{24}	3.794×10^{27}
7	-2.713×10^{26}	2.823×10^{30}
6	6.901×10^{29}	2.716×10^{33}
5	1.634×10^{33}	1.857×10^{36}
4	5.468×10^{35}	5.193×10^{38}
3	-8.532×10^{37}	1.824×10^{41}
2	-4.845×10^{40}	2.796×10^{43}
1	-9.488×10^{40}	5.945×10^{44}
0	1.118×10^{43}	7.926×10^{46}

Table B.6
Controller parameters for the non-collocated beam case study.

Parameter	PPF	NPF	NBP	NBP
g	38.5	37.9	—	—
M	—	—	86	86
n	—	—	1	2
m	—	—	0	0
ζ_c	0.22	0.22	0.148	0.385
$\omega_c/(2\pi)$ (Hz)	53.7	53.7	53.7	53.7
ω_d (rad/s)	341	393	12.5	14
σ	−1	−1	+1	+1

References

Balas, M. J. (1978). Active control of flexible systems. *Journal of Optimization Theory and Applications*, *25*(3), 415–436.

Bhikkaji, B., Ratnam, M., & Moheimani, S. O. R. (2007). PVPF control of piezoelectric tube scanners. *Sensors and Actuators A: Physical*, *135*(2), 700–712.

Cazzulani, G., Resta, F., Ripamonti, F., & Zanzi, R. (2012). Negative derivative feedback for vibration control of flexible structures. *Smart Materials and Structures*, *21*(7), 075024.

Chen, Z., Zhong, X., Shi, J., & Zhang, X. (2021). Damping-enabling technologies for broadband control of piezo-stages: A survey. *Annual Reviews in Control*, *52*, 120–134.

Debattisti, N., Cinquemani, S., & Zanelli, F. (2023). Automatic decentralized vibration control system based on collaborative stand-alone smart dampers. *Applied Sciences*, *13*(6), 3406.

Ebeling, D., & Solares, S. D. (2013). Bimodal atomic force microscopy driving the higher eigenmode in frequency-modulation mode: Implementation, advantages, disadvantages and comparison to the open-loop case. *Beilstein Journal of Nanotechnology*, *4*(1), 198–207.

Fanson, J. L., & Caughey, T. K. (1990). Positive position feedback control for large space structures. *AIAA Journal*, *28*(4), 717–724.

Fleming, A. J. (2009). Nanopositioning system with force feedback for high-performance tracking and vibration control. *IEEE/ASME Transactions on Mechatronics*, *15*(3), 433–447.

Heertjes, M. F., Butler, H., Dirkx, N. J., van der Meulen, S. H., Ahlawat, R., O'Brien, K., Simonelli, J., Teng, K.-T., & Zhao, Y. (2020). Control of wafer scanners: Methods and developments. In *2020 American control conference (ACC)* (pp. 3686–3703). IEEE.

Housner, G., Bergman, L. A., Caughey, T. K., Chassiakos, A. G., Claus, R. O., Masri, S. F., Skelton, R. E., Soong, T. T., Spencer, B. F., & Yao, J. T. P. (1997). Structural control: Past, present, and future. *Journal of Engineering Mechanics*, *123*(9), 897–971.

Hyodo, Y., & Yabuno, H. (2023). Self-excited microcantilever with higher mode using band-pass filter. *Sensors*, *23*(5), 2849.

Jamshidi, R., & Collette, C. (2022a). Designing negative derivative feedback controller based on maximum damping and H 2 method. *Smart Materials and Structures*, *31*(7), 075023.

Jamshidi, R., & Collette, C. (2022b). Optimal negative derivative feedback controller design for collocated systems based on H2 and H∞ method. *Mechanical Systems and Signal Processing*, *181*, 109497.

Kaczmarek, M. B., & HosseinNia, S. H. (2024). Creating bandgaps in active piezoelectric slender beams through positive position feedback control. *Smart Materials and Structures*, *33*(12), 125039.

Li, L., Li, C.-X., Gu, G., & Zhu, L.-M. (2017). Positive acceleration, velocity and position feedback based damping control approach for piezo-actuated nanopositioning stages. *Mechatronics*, *47*, 97–104.

Ling, J., Rakotondrabe, M., Feng, Z., Ming, M., & Xiao, X. (2019). A robust resonant controller for high-speed scanning of nanopositioners: Design and implementation. *IEEE Transactions on Control Systems Technology*, *28*(3), 1116–1123.

Liu, Z., Yao, Z., Li, X., & Fu, Q. (2016). Design and experiments of a linear piezoelectric motor driven by a single mode. *Review of Scientific Instruments*, *87*(11), 115001.

Natu, A., & Hosseinnia, H. (2026a). Non-minimum-phase resonant controller for active damping control: Application to piezo-actuated nanopositioning system. *Control Engineering Practice*, *169*. https://doi.org/10.1016/j.conengprac.2026.106790

Natu, A., & HosseinNia, H. (2026b). Nonminimum-phase-based loop shaping for multimode active damping control: Application to piezoelectric nanopositioning system. *Journal of Vibration and Acoustics*, *148*(6), 061002.

Oomen, T. (2018). Advanced motion control for precision mechatronics: Control, identification, and learning of complex systems. *IEEJ Journal of Industry Applications*, *7*(2), 127–140.

Pawlenka, M., Mahdal, M., Tuma, J., & Burecek, A. (2019). Application of a bandpass filter for the active vibration control of high-speed rotors. *International Journal of Acoustics and Vibration*, *24*(3), 608–615.

Preumont, A. (2002). Vibration control of active structures: An introduction. Springer.

Song, X., Zheng, S., Han, B., Peng, C., & Zhou, X. (2016). Active damping stabilization for high-speed BLDCM drive system based on band-pass filter. *IEEE Transactions on Power Electronics*, *32*(7), 5438–5449.

Wu, Y., Zhang, W., Meng, X., & Su, Y. (2018). Compensated positive position feedback for active control of piezoelectric structures. *Journal of Intelligent Material Systems and Structures*, *29*(3), 397–410.

Zhu, T., Liu, B., Zhang, H.-T., & Chen, Z. (2016). A design of novel damping controller combined with PID for nanopositioners. In *2016 35th Chinese control conference (CCC)* (pp. 4539–4544). IEEE.



Aditya Natu received the MSc in Mechanical Engineering (*cum laude*) with a specialization in Mechatronics System Design and is currently employed as a PhD Candidate at the Department of Precision and Microsystems Engineering, Delft University of Technology, Delft, The Netherlands. His research interests include active damping control, distributed actuation and sensing, precision mechatronics, and nanopositioning systems.



Dr. Hassan HosseinNia received his Ph.D. degree cum laude in Electrical Engineering in 2013, specializing in automatic control and its applications in mechatronics. He is currently a faculty member at Delft University of Technology (TU Delft), where he leads advanced research in precision mechatronic system design, high-performance motion control, active vibration damping, and the design and control of electromagnetic and piezoelectric actuators. His contributions have been recognized internationally. In 2024, he received the Abel Young Scientists Award from the 12th IFAC Conference on Fractional Differentiation and its Applications. His current research focuses on developing innovative control strategies and system architectures to enhance bandwidth and precision in next-generation mechatronic systems. He has published extensively in leading journals and conferences. Dr. HosseinNia served as the General Chair of the 7th IEEE International Conference on Control, Mechatronics, and Automation (ICCMA 2019). He also serves on the editorial boards of Mechatronics, Control Engineering Practice, and Fractional Calculus and Applied Analysis. Through his work, Dr. Hosseinnia brings a forward-looking perspective that bridges theoretical depth with industrial applicability, fostering innovation in advanced control and mechatronic system design.